J Eng Math (2008) 61:249–269
DOI 10.1007/s10665-008-9216-4

Thermomechanical behavior of polarizable and magnetizable electroconductive solids subjected to induction heating

B. Drobenko · O. Hachkevych · T. Kournyts'kyi

Received: 31 October 2006 / Accepted: 28 January 2008 / Published online: 20 February 2008

Abstract This paper presents a mathematical and numerical model developed for coupled time-dependent electromagnetic, temperature and mechanical processes, which occur in polarizable and magnetizable electroconductive solids subjected to an electromagnetic field generated by external currents. The electromagnetic field in the solid and in its surroundings is described by Maxwell's equations. The temperature variation in the solid is governed by the classical heat-transfer equation. To predict the stress–strain state of the solid, a nonisothermal theory for thermoplastic materials is used. The model takes into account the temperature dependence of all material coefficients and the nonlinear dependence of the induction on the strength of both the electrical and the magnetic fields. The problem is solved by a finite-element method and a unified set of single time-step algorithms. As an example, the process of high-temperature induction heating of a finite cylinder is considered.

Keywords Finite-element method · High-temperature induction heating · Process coupling · Thermo-mechanics

1 Introduction

Electromagnetic fields are widely used in modern technologies with the aim of improving the strength and reliability of solid materials. In particular, induction heating is frequently applied for hardening, quenching, tempering, brazing and other heat-processing techniques and demands very accurate control of heated depth and surface areas. Therefore, to develop rational heating regimes, the in-depth investigation of coupled electrical, thermal and mechanical processes in solid materials upon the material's polarizable and magnetizable properties is of high importance.

In classical models dealing with modeling deformation in electroconductive solids, the material properties are treated as temperature-independent and only elastic deformation is taken into account. Such models are not expected to predict correct results when a solid is heated to high temperatures. The behavior of most materials during heat treatment is nonlinear and very complex. For example, carbon steel undergoes plastic deformations [1] already at temperatures around 550–600°C. Its electrical conductivity in the temperature range 20–900°C can change by a factor of 6–8 and the magnetic permeability even by several orders [2]. Moreover, electroconductive materials can

B. Drobenko (✉) · O. Hachkevych · T. Kournyts'kyi
Institute for Applied Problems of Mechanics and Mathematics, Ukrainian National Academy of Sciences,
Naukova Str. 3b, Lviv 79060, Ukraine
e-mail: budz@iapmm.lviv.ua

be magnetized or polarized during the process of heat treatment. Therefore, more adequate mathematical models are to be developed to capture coupled thermal, mechanical and electromagnetic processes in electroconductive solids in a wide temperature range, accounting for nonlinearity of the material properties.

In most recent work in the field of induction heating the coupling of only electromagnetic and thermal processes is considered [3–9]. Simultaneous consideration of electromagnetic, thermal and elastic processes in composite solids subjected to magnetic fields are examined in [10–13] while taking into account the geometrical nonlinearity. In [14–16] the effect of induction heating on the thermomechanical behavior of axi-symmetric thermosensitive elastic and elasto–plastic magnetically soft ferromagnetic solids is investigated.

In this paper a mathematical model and an approach to a numerical simulation of coupled mechanical, thermal and electromagnetic processes in electroconductive solids subjected to an external electromagnetic field is developed. The model accounts for thermo–elasto–plastic deformation of the thermally sensitive solid as well as the nonlinear dependence of induction on the strength of both the electrical and the magnetic fields. The electromagnetic field in the solid and in its surroundings is described by Maxwell's equations. The temperature evolution in the solid is governed by the classical heat-transfer equation. The stress–strain state of the solid is computed within the nonisothermal theory for thermo–elastic–plastic materials.

2 The mathematical problem

Consider an electroconductive solid occupying the domain $\Omega \in E^3$ (with no electric charges and currents inside), whose surface Γ is Lipschitz-continuous. The solid is subjected to an electromagnetic field produced by a set of currents of density $\mathbf{j}^{(0)}(\mathbf{r}, t)$ ($\mathbf{r}$ is the radius-vector) distributed in a finite region of surroundings ($E^3 \backslash \Omega$).

Let us pose the problem of determining the electromagnetic field, the temperature and stress–strain state in the solid for given thermal and mechanical boundary and initial conditions. The electromechanical, thermo-electric and magnetostriction effects are neglected and the solid is assumed to be at rest. Suppose the frequency of the electromagnetic field is not close to resonance so that the deformation can be treated as quasistatic. Suppose also that the electric- and magnetic-field inductions are nonlinear functions of the corresponding strengths while the strength and induction vectors are parallel. The effect of the external electromagnetic field on heat transfer and deformation is modelled by heat sources and bulk (ponderomotive) forces. Joule heat sources, as well as those due to repolarization and remagnetization are considered.

The model will take into account the temperature dependence of all material properties. In the numerical investigation these dependencies will be approximated by interpolation splines constructed by real curves describing temperature behavior of a solid in an electromagnetic field during the entire heating–cooling range.

2.1 The electromagnetic model

The electromagnetic field in the solid in the case of the state equations

$$\mathbf{D}^{(0)} = \varepsilon_0 \mathbf{E}^{(0)}, \quad \mathbf{D}^{(1)} = \mathbf{D}_*^{(1)}(\mathbf{E}^{(1)}, T), \quad \mathbf{B}^{(0)} = \mu_0 \mathbf{H}^{(0)}, \quad \mathbf{B}^{(1)} = \mathbf{B}_*^{(1)}(\mathbf{H}^{(1)}, T), \quad \mathbf{j}^{(1)} = \gamma_* \mathbf{E}^{(1)}, \tag{1}$$

is described by Maxwell's equations:

$$\vec{\nabla} \times \mathbf{H}^{(m)} = \frac{\partial \mathbf{D}^{(m)}}{\partial t} + \mathbf{j}^{(m)}, \tag{2}$$

$$\vec{\nabla} \times \mathbf{E}^{(m)} = -\frac{\partial \mathbf{B}^{(m)}}{\partial t}, \tag{3}$$

$$\vec{\nabla} \cdot \mathbf{D}^{(m)} = 0, \quad \mathbf{r} \in E^3, \tag{4}$$

where $\mathbf{E} = (E_1, E_2, E_3)^T$, $\mathbf{H} = (H_1, H_2, H_3)^T$, $\mathbf{D} = (D_1, D_2, D_3)^T$, $\mathbf{B} = (B_1, B_2, B_3)^T$ denote the strengths and inductions of the electric and magnetic fields, respectively (index "T" denotes the transpose); $\mathbf{D}_* = (D_{*1}, D_{*2}, D_{*3})^T$,

$\mathbf{B}_* = (B_{*1}, B_{*2}, B_{*3})^T$ are, in general, nonlinear functions relating induction and strength vectors for the electric and magnetic fields in a solid, respectively (in fact, these functions represent polarization and magnetization curves), T is the temperature, ε_0, μ_0 are the dielectric and magnetic permeabilities of vacuum (the surrounding medium is assumed to have the electromagnetic properties of the vacuum); $\mathbf{j}$ is the current density, γ_* is the tensor of electrical conductivity of a solid, $\vec{\nabla} = (\nabla_1, \nabla_2, \nabla_3)$ is Hamilton's operator; $(\vec{\nabla}\times)$, $(\vec{\nabla}\cdot)$ denote curl and divergence, respectively. The index $m = 0$ refers to the surrounding medium and index $m = 1$ refers to the solid.

Let us reduce the basic correlations (2)–(4) for an electroconductive solid to a set of equations written with respect to the electric-field-strength vector $\mathbf{E}$. Substitution of Eq. (1) in (2)–(4) yields for the solid

$$\vec{\nabla} \times \mathbf{H}^{(1)} = [\varepsilon_*] \frac{\partial \mathbf{E}^{(1)}}{\partial t} + \frac{\partial \mathbf{D}_*^{(1)}}{\partial T} \frac{\partial T}{\partial t} + \gamma_* \mathbf{E}^{(1)}, \tag{5}$$

$$\vec{\nabla} \times \mathbf{E}^{(1)} = -[\mu_*] \frac{\partial \mathbf{H}^{(1)}}{\partial t} - \frac{\partial \mathbf{B}_*^{(1)}}{\partial T} \frac{\partial T}{\partial t}, \tag{6}$$

$$\vec{\nabla} \cdot \left(\mathbf{D}_*^{(1)}(\mathbf{E}^{(1)}, \mathrm{T}) \right) = 0, \quad \mathbf{r} \in \Omega. \tag{7}$$

Since the induction and strength vectors are parallel, we have

$$[\varepsilon_*] = \begin{bmatrix} \varepsilon_{11} & 0 & 0 \\ 0 & \varepsilon_{22} & 0 \\ 0 & 0 & \varepsilon_{33} \end{bmatrix}, \quad \varepsilon_{ii} = \frac{\partial D_{*i}^{(1)}}{\partial E_i^{(1)}}, \quad [\mu_*] = \begin{bmatrix} \mu_{11} & 0 & 0 \\ 0 & \mu_{22} & 0 \\ 0 & 0 & \mu_{33} \end{bmatrix}, \quad \mu_{ii} = \frac{\partial B_{*i}^{(1)}}{\partial H_i^{(1)}}, \quad i = 1, 2, 3.$$

If the materials are isotropic, the matrices $[\varepsilon_*]$ and $[\mu_*]$ are reduced to diagonal ones:

$$[\varepsilon_*] = \begin{bmatrix} \varepsilon & 0 & 0 \\ 0 & \varepsilon & 0 \\ 0 & 0 & \varepsilon \end{bmatrix}, \quad \varepsilon = \frac{\partial |\mathbf{D}_*|}{\partial |\mathbf{E}^{(1)}|}, \quad [\mu_*] = \begin{bmatrix} \mu & 0 & 0 \\ 0 & \mu & 0 \\ 0 & 0 & \mu \end{bmatrix}, \quad \mu = \frac{\partial |\mathbf{B}_*|}{\partial |\mathbf{H}^{(1)}|},$$

where ε, μ are the differential dielectric and magnetic permeabilities of the solid, which are directly derived—at a given temperature—from the magnetization and polarization curves, respectively.

Multiply Eq. (6) by $[\mu_*]^{-1}$ and apply the curl$(\vec{\nabla}\times)$ to it:

$$\vec{\nabla} \times \left([\mu_*]^{-1} \vec{\nabla} \times \mathbf{E}^{(1)} \right) + \vec{\nabla} \times \frac{\partial \mathbf{H}^{(1)}}{\partial t} = -\vec{\nabla} \times \left([\mu_*]^{-1} \frac{\partial \mathbf{B}_*^{(1)}}{\partial T} \frac{\partial T}{\partial t} \right). \tag{8}$$

Let us change the order of the operations curl and $\frac{\partial}{\partial t}$ and substitute Eq. (5) in Eq. (8):

$$\vec{\nabla} \times \left([\mu_*]^{-1} \vec{\nabla} \times \mathbf{E}^{(1)} \right) + \frac{\partial}{\partial t} \left([\varepsilon_*] \frac{\partial \mathbf{E}^{(1)}}{\partial t} + \frac{\partial \mathbf{D}_*^{(1)}}{\partial T} \frac{\partial T}{\partial t} + \gamma_* \mathbf{E}^{(1)} \right) = -\vec{\nabla} \times \left([\mu_*]^{-1} \frac{\partial B_*^{(1)}}{\partial T} \frac{\partial T}{\partial t} \right). \tag{9}$$

Carrying out the time differentiation in the last equation, we obtain an equation written in terms of the electric-field strength:

$$\vec{\nabla} \times \left([\mu_*]^{-1} \vec{\nabla} \times \mathbf{E}^{(1)} \right) + \frac{\partial \gamma_*}{\partial t} \mathbf{E}^{(1)} + \mathbf{F}_\gamma \frac{\partial \mathbf{E}^{(1)}}{\partial t} + [\varepsilon_*] \frac{\partial^2 \mathbf{E}^{(1)}}{\partial t^2} = \mathbf{F}_B. \tag{10}$$

Here

$$\mathbf{F}_\gamma = \gamma_* + 2\mathbf{D}_{*ET} \frac{\partial T}{\partial t} + \mathbf{D}_{*EE}, \quad \mathbf{F}_B = -\frac{\partial^2 \mathbf{D}_*^{(1)}}{\partial T^2} \left(\frac{\partial T}{\partial t} \right)^2 - \frac{\partial \mathbf{D}_*^{(1)}}{\partial T} \frac{\partial^2 T}{\partial t^2} - \vec{\nabla} \times \left([\mu_*]^{-1} \frac{\partial \mathbf{B}_*^{(1)}}{\partial T} \frac{\partial T}{\partial t} \right).$$

The elements of the matrices $\mathbf{D}_{*ET}$ and $\mathbf{D}_{*EE}$ are as follows:

$$[\mathbf{D}_{*ET}]_{ii} = \frac{\partial \varepsilon_{ii}}{\partial T}, \quad [\mathbf{D}_{*EE}]_{ii} = \frac{\partial^2 D_i}{\partial^2 E_i^{(1)}} \frac{\partial E_i^{(1)}}{\partial t}.$$

Note that in the case of a harmonic quasi-steady external electromagnetic field, that is, when $\gamma >> \varepsilon\omega$, the displacement currents are negligible compared to conduction currents in a solid [17]. This is the case for the range of frequencies typically used in an industrial set-up when dealing with highly conductive solids. Hence Eq. (10) becomes a parabolic-type equation:

$$\vec{\nabla} \times \left([\mu_*]^{-1} \vec{\nabla} \times \mathbf{E}^{(1)} \right) + \frac{\partial \gamma_*}{\partial t} \mathbf{E}^{(1)} + \gamma_* \frac{\partial \mathbf{E}^{(1)}}{\partial t} = -\vec{\nabla} \times \left([\mu_*]^{-1} \frac{\partial \mathbf{B}_*^{(1)}}{\partial T} \frac{\partial T}{\partial t} \right). \tag{11}$$

The corresponding equation for the surrounding medium is as follows:

$$\vec{\nabla} \times (\mu_0^{-1} \vec{\nabla} \times \mathbf{E}^{(0)}) + \varepsilon_0 \frac{\partial^2 \mathbf{E}^{(0)}}{\partial t^2} = -\frac{\partial \mathbf{j}^{(0)}}{\partial t}. \tag{12}$$

The electric-field strength in a system solid-surroundings being known, the magnetic field induction is found from the relation

$$\mathbf{B}^{(m)} = -\int_0^t \vec{\nabla} \times \mathbf{E}^{(m)} \mathrm{d}t', \tag{13}$$

while the electric-field induction $\mathbf{D}$ and the magnetic field strength $\mathbf{H}$ as well as the dielectric $[\varepsilon_*]$ and magnetic $[\mu_*]$ permeabilities of the solid at each moment of time are calculated from the constitutive equation (1) according to the magnetization and polarization curves.

Suppose at initial moment of time there is no electromagnetic field in the system, that is,

$$\mathbf{E}^{(m)}(\mathbf{r}, 0) = \frac{\partial \mathbf{E}^{(m)}(\mathbf{r}, 0)}{\partial t} = 0, \quad \mathbf{r} \in E^3. \tag{14}$$

The common practice is to start with the integral form of Maxwell's equations in establishing correlations for the electromagnetic-field characteristics on the solid-surrounding interface Γ. Provided interface currents are absent, these correlations yield two independent conditions expressing equality of the tangential components of the electric- and magnetic-field-strength vectors on the interface [18]. In our case these conditions are

$$\mathbf{n} \times (\mathbf{E}^{(1)} - \mathbf{E}^{(0)}) = 0, \tag{15}$$

$$\mathbf{n} \times \left([\mu_*]^{-1} \vec{\nabla} \times \mathbf{E}^{(1)} - \mu_0^{-1} \vec{\nabla} \times \mathbf{E}^{(0)} \right) = 0, \tag{16}$$

where $\mathbf{n}$ is the unit vector normal to the solid's surface Γ.

Suppose the following condition [18] is fulfilled at the infinity

$$\lim_{|\mathbf{r}| \to \infty} |\mathbf{r}| \left| \mathbf{E}^{(0)} \right| = \text{const}. \tag{17}$$

The Maxwell equations can be written in terms of the magnetic-field-strength vector $\mathbf{H}$. In the case of a quasi-steady external electromagnetic field for the solid they become

$$\left(\vec{\nabla} \times \left(\gamma_*^{-1} \vec{\nabla} \times \mathbf{H} \right) \right) + [\mu_*] \frac{\partial \mathbf{H}}{\partial t} = -\frac{\partial \mathbf{B}}{\partial T} \frac{\partial T}{\partial t}, \tag{18}$$

$$\mathbf{E} = \gamma_*^{-1} \vec{\nabla} \times \mathbf{H}, \tag{19}$$

$$\vec{\nabla} \cdot \mathbf{B}_*(\mathbf{H}, T) = 0, \quad \mathbf{r} \in \Omega. \tag{20}$$

Boundary and initial conditions are constructed in the same way as in the case when the Maxwell equations are written in terms of the electric-field strength.

2.2 The thermal model

The temperature field in the solid is described by the equation:

$$c\frac{\partial T}{\partial t} = \vec{\nabla}\cdot\left(\lambda\vec{\nabla}T\right) + Q, \quad \mathbf{r}\in\Omega. \tag{21}$$

Here $c = c(T)$ denotes the heat capacity; $\lambda = \lambda(T)$ is the coefficient of heat conduction; Q is the heat-source power. For a quasi-steady electromagnetic field far from resonance frequency, the temperature field can be calculated using heat sources averaged over the electromagnetic-wave period T_ω [19]:

$$Q = \frac{1}{T_\omega}\int_t^{t+T_w}\left(\mathbf{j}\cdot\mathbf{E} + \mathbf{H}\frac{\partial\mathbf{B}}{\partial t} + \mathbf{E}\frac{\partial\mathbf{D}}{\partial t}\right)\mathrm{d}t. \tag{22}$$

Note that the first term in (22) characterises Joule heat sources; the second and third terms are heat sources due to remagnetization and repolarization, respectively.

Suppose at an initial moment of time the temperature in the solid is defined in term of the function $T_0(\mathbf{r})$:

$$T(\mathbf{r},0) = T_0(\mathbf{r}), \quad \mathbf{r}\in\Omega \tag{23}$$

and the solid undergoes convective heat exchange with the surroundings through the interface Γ:

$$\lambda\mathbf{n}\cdot\vec{\nabla}T + \beta(T - T_S) = 0, \quad \mathbf{r}\in\Gamma, \tag{24}$$

where $\beta = \beta(T)$ denotes the heat-transfer coefficient; T_S is the temperature of the surroundings.

2.3 The mechanical model

The elasto–plastic state of the solid is described by the nonisothermal theory of thermoplastic materials [20]. The key equations of the theory are written in terms of increments while the plastic deformation is considered in a step-by-step fashion.

We assume that the plastic deformation occurs when the point σ_{ij} in stress space appears on the yield surface

$$\Phi(\sigma_{ij} - o_{ij}) = K^2\left(\int \mathrm{d}\bar{\varepsilon}_p, T\right), \tag{25}$$

where σ_{ij} are stress-tensor components; o_{ij} are the coordinates of the yield surface centre in stress space; K^2 is a function defining the size of the yield surface depending on the temperature and the accumulated plastic deformation $\int \mathrm{d}\bar{\varepsilon}_p$; $\mathrm{d}\bar{\varepsilon}_p = \sqrt{\frac{2}{3}\mathrm{d}\varepsilon^p_{ij}\mathrm{d}\varepsilon^p_{ij}}$ is the intensity of the plastic-deformation increments. Also

$$\Phi(\sigma_{ij}) = \left(1.5\cdot s_{ij}s_{ij}\right)^{0.5}, \quad s_{ij} = \sigma_{ij} - \delta_{ij}\sigma_{ii}/3, \tag{26}$$

where δ_{ij} is the Kronecker delta.

The increments of the stress-tensor components during load step $[t, t+\mathrm{d}t]$ are written as:

$$\mathrm{d}\sigma_{ij} = G^{t+\mathrm{d}t}_{ijkl}(\mathrm{d}\varepsilon_{kl} - \mathrm{d}\varepsilon^T_{kl} - \mathrm{d}\varepsilon^p_{kl}) + \mathrm{d}G_{ijkl}(\varepsilon_{kl} - \varepsilon^T_{kl} - \varepsilon^p_{kl}). \tag{27}$$

Here G^{t+dt}_{ijkl}, $\mathrm{d}G_{ijkl}$ are values of the elastic-modulus components at the time $t+\mathrm{d}t$ (at the end of the loading step) and their increments at a given step, correspondently; ε_{kl}, ε^T_{kl}, ε^p_{kl} are components of the total-strain, thermal-strain and plastic-strain tensors at the time t (at the beginning of the step).

To calculate the increments of the plastic strain, the associated flow rule describing growth of the plastic strains normally to the yield surface reads:

$$\mathrm{d}\varepsilon^p_{ij} = \mathrm{d}\chi\frac{\partial\Phi}{\partial\sigma_{ij}}. \tag{28}$$

The increments of the thermal strains are calculated as follows

$$\mathrm{d}\varepsilon_{ij}^{T} = \delta_{ij}(\alpha^{t+\mathrm{d}t}\mathrm{d}T + (\alpha^{t+\mathrm{d}t} - \alpha)(T - T_0)), \tag{29}$$

where $\alpha^{t+\mathrm{d}t}$, α^{t} are the thermal-expansion coefficient at the corresponding moments of time.

During the deformation process the yield surface can move in the stress state as well as change its shape. In this case the increment of the surface-centre coordinates is determined by the correlation [20]

$$\mathrm{d}o_{ij} = \mathrm{d}a(\sigma_{ij} - o_{ij}), \tag{30}$$

where $\mathrm{d}a$, using condition $\mathrm{d}\Phi = 0$ is given by

$$\mathrm{d}a = \left(\mathrm{d}\sigma_{ij}\frac{\partial\Phi}{\partial\sigma_{ij}} - 2K\frac{\partial K}{\partial\bar{\varepsilon}_i^p}\mathrm{d}\bar{\varepsilon}_i^p - 2K\frac{\partial K}{\partial T}\mathrm{d}T\right)\left((\sigma_{ij} - o_{ij})\frac{\partial\Phi}{\partial\sigma_{ij}}\right)^{-1}. \tag{31}$$

Taking into account the expressions (24)–(30), the correlations between increments of stresses and strains take the form [20]

$$\begin{aligned}\mathrm{d}\sigma_{ij} = {} & \left(G_{ijmn}^{t+\mathrm{d}t} - \frac{G_{ijvw}^{t+\mathrm{d}t}\frac{\partial\Phi}{\partial\sigma_{vw}}\frac{\partial\Phi}{\partial\sigma_{kl}}G_{klmn}^{t+\mathrm{d}t}}{\frac{2}{3}H^t\frac{\partial\Phi}{\partial\sigma_{pq}}\frac{\partial\Phi}{\partial\sigma_{pq}} + G_{pqrs}^{t+\mathrm{d}t}\frac{\partial\Phi}{\partial\sigma_{pq}}\frac{\partial\Phi}{\partial\sigma_{rs}}}\right)\left(\mathrm{d}\varepsilon_{mn} - \mathrm{d}\varepsilon_{mn}^{T}\right) \\ & + \left(\mathrm{d}G_{ijmn} - \frac{G_{ijvw}^{t+\mathrm{d}t}\frac{\partial\Phi}{\partial\sigma_{vw}}\frac{\partial\Phi}{\partial\sigma_{kl}}\mathrm{d}G_{klmn}}{\frac{2}{3}H^t\frac{\partial\Phi}{\partial\sigma_{pq}}\frac{\partial\Phi}{\partial\sigma_{pq}} + G_{pqrs}^{t+\mathrm{d}t}\frac{\partial\Phi}{\partial\sigma_{pq}}\frac{\partial\Phi}{\partial\sigma_{rs}}}\right)\left(\varepsilon_{mn} - \varepsilon_{mn}^{p} - \varepsilon_{mn}^{T}\right) \\ & + \frac{\sqrt{\frac{2}{3}\frac{\partial\Phi}{\partial\sigma_{kl}}\frac{\partial\Phi}{\partial\sigma_{kl}}}G_{ijmn}^{t+\mathrm{d}t}\frac{\partial\Phi}{\partial\sigma_{mn}}\frac{\partial\sigma_i}{\partial T}}{\frac{2}{3}H^t\frac{\partial\Phi}{\partial\sigma_{pq}}\frac{\partial\Phi}{\partial\sigma_{pq}} + G_{pqrs}^{t+\mathrm{d}t}\frac{\partial\Phi}{\partial\sigma_{pq}}\frac{\partial\Phi}{\partial\sigma_{rs}}}\mathrm{d}T,\end{aligned}$$

or in matrix form:

$$\{\mathrm{d}\sigma\} = [\mathbf{C}]^{t+\Delta t}(\{\mathrm{d}\varepsilon\} - \{\mathrm{d}\varepsilon_T\}) + [\mathrm{d}\mathbf{C}](\{\varepsilon\} - \{\varepsilon_T\} - \{\varepsilon_p\}) + \{Z\}\mathrm{d}T. \tag{32}$$

Here H^t is the instantaneous slope of the stress–plastic–strain diagram, while the components of the strain and stress tensors are given by the vectors [21]

$$\{\varepsilon\} = (\varepsilon_{11}, \varepsilon_{22}, \varepsilon_{33}, 2\varepsilon_{12}, 2\varepsilon_{13}, 2\varepsilon_{23})^T, \quad \{\sigma\} = (\sigma_{11}, \sigma_{22}, \sigma_{33}, \sigma_{12}, \sigma_{13}, \sigma_{23})^T.$$

Note that the last two terms of Eq. (32) describe the dependencies of the elastic material properties and yielding limit of a material on the temperature. The terms H^t and $\frac{\mathrm{d}\sigma_i}{\mathrm{d}T}$ may be determined from uniaxial stress–strain data at time t.

The set of model equations is to be completed by geometric correlations (considering small deformations only) and equilibrium equations [21]:

$$\{\varepsilon\} = [\mathbf{A}]\mathbf{u}, \qquad [\mathbf{A}]^T\{\sigma\} + \mathbf{F} = 0, \qquad \mathbf{r} \in \Omega \tag{33,34}$$

and known boundary conditions

$$[\Sigma_n]^T\{\sigma\} = \mathbf{p}, \quad \mathbf{r} \in \Gamma_\sigma, \quad \mathbf{u} = \mathbf{u}_0, \quad \mathbf{r} \in \Gamma_u, \quad \Gamma_\sigma \cap \Gamma_u = \emptyset; \quad \Gamma_\sigma \cup \Gamma_u = \partial\Omega. \tag{35}$$

Here

$$[\mathbf{A}] = \begin{bmatrix} \nabla_1 & 0 & 0 & \nabla_2 & \nabla_3 & 0 \\ 0 & \nabla_2 & 0 & \nabla_1 & 0 & \nabla_3 \\ 0 & 0 & \nabla_3 & 0 & \nabla_1 & \nabla_2 \end{bmatrix}^T, \quad [\Sigma_n] = \begin{bmatrix} n_1 & 0 & 0 & n_2 & n_3 & 0 \\ 0 & n_2 & 0 & n_1 & 0 & n_3 \\ 0 & 0 & n_3 & 0 & n_1 & n_2 \end{bmatrix}^T$$

are correspondently the matrices of the differential operator of geometric correlations in linear elasticity and the unit vector of the external normal to the surface Γ_σ; $\mathbf{u} = (u_1, u_2, u_3)^T$ is the displacement vector; $\mathbf{p}$ is the mechanical-load vector on the surface Γ_σ; $\mathbf{u}_0$ denotes the displacement vectors defined on the surface Γ_u; $\mathbf{F}$ is the vector

of bulk (ponderomotive) forces. The adopted assumptions regarding quasi-steadiness of the electromagnetic field lead to the following expression for the ponderomotive forces [19]

$$\mathbf{F} = \frac{1}{T_\omega}\int_t^{t+T_\omega} (\mathbf{j}\times\mathbf{B} + (\mathbf{P}\cdot\vec{\nabla})\cdot\mathbf{E} + (\mathbf{M}\cdot\vec{\nabla})\cdot\mathbf{B} + \mathbf{M}\times(\vec{\nabla}\times\mathbf{B}))\mathrm{d}t, \tag{36}$$

where $\mathbf{P}$, $\mathbf{M}$ are the polarization and magnetization vectors. Taking into account Eq. (1), they are written as

$$\mathbf{P}(\mathbf{E},\mathrm{T}) = \mathbf{D}_*(\mathbf{E},\mathrm{T}) - \varepsilon_0\mathbf{E}, \quad \mathbf{M}(\mathbf{H},\mathrm{T}) = \mu_0^{-1}\mathbf{B}_*(\mathbf{H},\mathrm{T}) - \mathbf{H}. \tag{37,38}$$

Note that the first and the last terms in Eq. (36) represent Ampere and Calvin forces, while the third and fourth stand for the forces acting on the magnetic dipoles.

2.4 Basic equations of the model

The numerical approach developed above for the determination of the stress–strain state of an electroconductive solid subjected to an electromagnetic field is split in two stages. The first stage deals with solving the coupled problem regarding electrodynamics and thermal conductivity. If the strength vector $\mathbf{E}$ is chosen as a basic function, the electromagnetic field in the system composed of solid and surroundings and the temperature distribution in the solid are determined by Eqs. (7), (10) and (21) for the solid Ω and (4) and (12) for the surroundings $E^3\backslash\Omega$ subject to the initial conditions (14), (23), the conditions (15), (16) and (24) on the interface Γ as well as by condition (17) at infinity. The magnetic-field induction $\mathbf{B}$ is then found from Eq. (13), while the electric-field induction $\mathbf{D}$ and magnetic-field strength $\mathbf{H}$, as well as the differential electric permeability $[\varepsilon_*]$ and magnetic permeability $[\mu_*]$ at each moment of time are determined from the material correlations (1).

The temperature and ponderomotive forces having been found, the displacements, stresses and strains are calculated from the system of thermo–elasto–plastic equations (32)–(35).

2.5 Axi-symmetrical case

Circular inductors are widely used for induction heating. Consider the case of an isotropic axisymmetric electroconductive solid in a cylindrical coordinate system (r, φ, z). The solid is subjected to an electromagnetic field generated by currents of density $\mathbf{j}^{(0)} = (0,\, j_\varphi^{(0)}(r,z,t),\, 0)$ that are coaxial with the solid located in a finite subdomain of surroundings.

As can be seen from the basic correlations, in this case only the angular component of the electric-field strength $E_\varphi(r,\ z, t)$ and two components $H_r(r,z,t)$, $H_z(r,z,t)$ of the magnetic-field strength $\mathbf{H}$, along with the corresponding components of the vectors $\mathbf{D}$ and $\mathbf{B}$, have nonzero values. Equation (7) for the solid and (4) for the surroundings are satisfied identically. Then Eqs. (10), (12) and (21) and the interface conditions (15), (16), (24) written in terms of E_φ, the only nonzero component of the electric-field-strength vector $\mathbf{E}$, take the form:

$$-\frac{\partial}{\partial r}\left(\mu^{-1}\frac{1}{r}\frac{\partial}{\partial r}\left(rE_\varphi^{(1)}\right)\right) - \frac{\partial}{\partial z}\left(\mu^{-1}\frac{\partial E_\varphi^{(1)}}{\partial z}\right) + \frac{\partial\gamma}{\partial t}E_\varphi^{(1)} + F_\gamma\frac{\partial E_\varphi^{(1)}}{\partial t} + \varepsilon\frac{\partial^2 E_\varphi^{(1)}}{\partial t^2} = F_B, \tag{39}$$

$$-\mu_0^{-1}\left(\frac{\partial}{\partial r}\left(\frac{1}{r}\frac{\partial}{\partial r}\left(rE_\varphi^{(0)}\right)\right) - \frac{\partial}{\partial z}\left(\frac{\partial E_\varphi^{(0)}}{\partial z}\right)\right) + \varepsilon_0\frac{\partial^2 E_\varphi^{(0)}}{\partial t^2} = -\frac{\partial j_\varphi}{\partial t}, \tag{40}$$

$$c\frac{\partial T}{\partial t} = \frac{1}{r}\frac{\partial}{\partial r}\left(\lambda r\frac{\partial T}{\partial r}\right) + \frac{\partial}{\partial z}\left(\lambda\frac{\partial T}{\partial z}\right) + Q, \quad (r,z)\in\Omega_2 \tag{41}$$

$$E_\varphi^{(0)} = E_\varphi^{(1)}, \tag{42}$$

$$\left(\mu^{-1}\frac{1}{r}\frac{\partial(rE_\varphi^{(1)})}{\partial r}-\mu_0^{-1}\frac{1}{r}\frac{\partial(rE_\varphi^{(0)})}{\partial r}\right)n_r+\left(\mu^{-1}\frac{\partial E_\varphi^{(1)}}{\partial z}-\mu_0^{-1}\frac{\partial E_\varphi^{(0)}}{\partial z}\right)n_z=0, \tag{43}$$

$$\lambda\left(\frac{\partial T}{\partial r}n_r+\frac{\partial T}{\partial z}n_z\right)+\beta(T-T_S)=0,\quad (r,z)\in\Gamma_2. \tag{44}$$

where Ω_2 is the meridional cross-section of the solid, $(n_r, n_z)^T$ is the unit vector of the normal to the surface $\Gamma_2=\partial\Omega_2$, μ and ε denote the differential magnetic and dielectric permeabilities, which are derived directly—at a given temperature—from the magnetization and polarization curves, given by functions $\mathbf{B}_*=(B_*,0,B_*)^T$ and $\mathbf{D}_*=(0,D_*,0)^T$, respectively; γ is the coefficient of electrical conductivity; then

$$F_\gamma=\gamma+2\frac{\partial\varepsilon}{\partial T}\frac{\partial T}{\partial t}+\frac{\partial\varepsilon}{\partial E_\varphi^{(1)}}\frac{\partial E_\varphi^{(1)}}{\partial t},$$

$$F_B=-\frac{\partial^2 D_*}{\partial T^2}\left(\frac{\partial T}{\partial t}\right)^2-\frac{\partial D_*}{\partial T}\frac{\partial^2 T}{\partial t^2}+\frac{\partial}{\partial z}\left(\mu^{-1}\frac{\partial B_*}{\partial T}\frac{\partial T}{\partial t}\right)-\frac{\partial}{\partial r}\left(\mu^{-1}\frac{\partial B_*}{\partial T}\frac{\partial T}{\partial t}\right).$$

The problem of determining the electromagnetic field in the system consisting of solid and surroundings and of the temperature field in the solid reduces to the solution of Eqs. (36), (38) for the solid and of (37) for the surroundings with zero initial value of the electric-field strength, given initial temperature distribution $T_0(r,z)$ in the solid, interface conditions (39)–(41), as well as the conditions $E_\varphi^{(m)}=0$ at infinity and at the z-axis, and the condition

$$\frac{\partial T(r,0,t)}{\partial r}=0,\quad (r,0)\in\Gamma_2. \tag{45}$$

In doing so, the components of the magnetic induction $\mathbf{B}$ are determined from

$$B_r^{(m)}=\int_0^t\frac{\partial E_\varphi^{(m)}}{\partial z}\mathrm{d}t',\quad B_z^{(m)}=-\int_0^t\frac{1}{r}\frac{\partial(rE_\varphi^{(m)})}{\partial r}\mathrm{d}t', \tag{46}$$

while the magnetic-field induction $\mathbf{H}$, as well as the differential magnetic permeability μ in the solid at each moment of time are calculated using the magnetization curve (1).

The temperature having been found, the equations of nonisothermal thermo-elastoplasticity (32)–(34), along with the boundary conditions (35) are used for the determination of the displacement $\mathbf{u}=(u_r,u_z)$, the strain $\{\varepsilon\}=\{\varepsilon_{rr},\varepsilon_{\varphi\varphi},\varepsilon_{zz},2\varepsilon_{rz}\}^T$ and the stress components $\{\sigma\}=\{\sigma_{rr},\sigma_{\varphi\varphi},\sigma_{zz},\sigma_{rz}\}^T$. In these equations the matrix of the differential operator for the geometric correlations and the matrix of the direction cosines of the external normal to the surface Γ_2 are as follows:

$$[\mathbf{A}]=\begin{bmatrix}\frac{\partial}{\partial r} & \frac{1}{r} & 0 & \frac{\partial}{\partial z}\\ 0 & 0 & \frac{\partial}{\partial z} & \frac{\partial}{\partial r}\end{bmatrix}^T,\quad [\Sigma_n]=\begin{bmatrix}n_r & 0 & n_z & 0\\ 0 & n_z & n_r & 0\end{bmatrix}^T.$$

If we had chosen the magnetic-field strength $\mathbf{H}$ as a key function for determining the electromagnetic field, we would have obtained two equations (with $H_r(r,z,t)$, $H_z(r,z,t)$ unknown) to be solved together with Eq. (41), instead of the single Eq. (39). However, if a long electroconductive cylinder is subjected to a quasi-steady external electromagnetic field independent of the z-coordinate, the only nonzero component H_z is determined from the following equation (neglecting displacement currents in the solid):

$$\frac{1}{r}\frac{\partial}{\partial r}\left(r\frac{1}{\gamma}\frac{\partial H_z^{(1)}}{\partial r}\right)-\mu\frac{\partial H_z^{(1)}}{\partial t}=\frac{\partial B_{*z}}{\partial T}\frac{\partial T}{\partial t}. \tag{47}$$

If the interface value of $H_z^{(1)}$ is known, the problem of determining the electromagnetic field and of the temperature in the cylinder reduces to the solution of Eqs. (47) and

$$c\frac{\partial T}{\partial t}=\frac{1}{r}\frac{\partial}{\partial r}\left(\lambda r\frac{\partial T}{\partial r}\right)+Q, \tag{48}$$

$$E_{\varphi}^{(1)} = \frac{1}{\gamma}\frac{\partial H_z^{(1)}}{\partial r}. \tag{49}$$

along with given boundary and initial conditions. The latter issue is discussed in more detail in [22].

3 The solution procedure

The solution of the above problem is carried out via the finite-element method [21] and a unified set of single-step algorithms [23]. In accordance with this procedure, the temperature and electromagnetic fields are determined first.

3.1 Finite-element equations for electromagnetic and temperature problems

Write down the key equations of the method of weighted residuals [24] assuming Eq. (4) to be fulfilled. With this in mind, let us multiply the heat-transfer equation (21) by the arbitrary weight function $w \in H^1(\Omega)$, where the Sobolev space is defined by $H^1(\Omega) = \{w \in L^2(\Omega), \nabla w \in L^2(\Omega)\}$ (L^2 is the Lebesgue space), and integrate the obtained equation over domain Ω:

$$\int_{\Omega}\left(c\frac{\partial \mathrm{T}}{\partial t} - \vec{\nabla}(\lambda\vec{\nabla}T) - Q\right) w_0 \mathrm{d}v = 0, \quad \forall w_0 \in H^1(\Omega). \tag{50}$$

Applying the standard transformations

$$\int_{\Omega}\vec{\nabla}(\lambda\vec{\nabla}T)w_0\mathrm{d}v = \int_{\Omega}\vec{\nabla}(\lambda\vec{\nabla}T\cdot w_0)\mathrm{d}v - \int_{\Omega}\lambda\vec{\nabla}T\cdot\vec{\nabla}w_0\mathrm{d}v = \int_{\Gamma}\lambda\mathbf{n}\cdot\vec{\nabla}T\cdot w_0\mathrm{d}s - \int_{\Omega}\lambda\vec{\nabla}T\cdot\vec{\nabla}w_0\mathrm{d}v \tag{51}$$

and taking into account the heat-transfer condition (24) for the thermal-conductivity problem, we obtain

$$\int_{V}\left(c\frac{\partial \mathrm{T}}{\partial t}w_0 + \lambda\vec{\nabla}T\cdot\vec{\nabla}w_0 - Qw_0\right)\mathrm{d}v + \int_{\Gamma}\beta\,(T - T_s)\,w_0\,\mathrm{d}s = 0, \quad \forall w_0 \in H^1(V). \tag{52}$$

Let us follow the same approach to Eqs. (10) and (12), substituting the infinite space by a finite volume V ($\Omega \subset V$) restricted by a surface S located far enough from the solid and given currents. Taking account of Gauss's formulae [25], we arrive at the equations

$$\int_{\Omega}\left([\mu_*]^{-1}(\vec{\nabla}\times\mathbf{E}^{(1)})(\vec{\nabla}\times\mathbf{w}) + \left(\frac{\partial\gamma_*}{\partial t}\mathbf{E}^{(1)} + \mathbf{F}_q\frac{\partial\mathbf{E}^{(1)}}{\partial t} + [\varepsilon_*]\frac{\partial^2\mathbf{E}^{(1)}}{\partial t^2} - \mathbf{F}_p\right)\mathbf{w}\right)\mathrm{d}v$$
$$+\int_{\Gamma}[\mu_*]^{-1}\left(\mathbf{n}\times(\vec{\nabla}\times\mathbf{E}^{(1)})\right)\mathbf{w}\,\mathrm{d}s = 0, \tag{53}$$

$$\int_{V\setminus\Omega}\left((\mu_0^{-1}\vec{\nabla}\times\mathbf{E}^{(0)})(\vec{\nabla}\times\mathbf{w}) + \left(\varepsilon_0\frac{\partial^2\mathbf{E}^{(0)}}{\partial t^2} + \frac{\partial\mathbf{j}^{(0)}}{\partial t}\right)\mathbf{w}\right)\mathrm{d}v$$
$$-\int_{\Gamma}\left(\mu_0^{-1}\mathbf{n}\times(\vec{\nabla}\times\mathbf{E}^{(0)})\right)\mathbf{w}\mathrm{d}s = 0, \quad \forall\mathbf{w}\in H(\vec{\nabla},V). \tag{54}$$

Here $H(\vec{\nabla},V) = \left\{\mathbf{w}\in\left(L^2(V)\right)^3, \vec{\nabla}\times\mathbf{w}\in\left(L^2(V)\right)^3 : \mathbf{w} = 0\forall\mathbf{r}\in S\right\}$, [25]. We get a "–" sign in Eq. (54) since $\mathbf{n}$ is an internal normal to surface Γ relative to the surroundings $V\setminus\Omega$.

Accounting for the boundary conditions (15), (16), we get an equation valid in the entire domain V:

$$\int_{V}\left(\mu_c^{-1}(\vec{\nabla}\times\mathbf{E})(\vec{\nabla}\times\mathbf{w}) + \left(\gamma_t\mathbf{E}^{(1)} + \mathbf{F}_c\frac{\partial\mathbf{E}}{\partial t} + \varepsilon_c\frac{\partial^2\mathbf{E}}{\partial t^2} - \mathbf{F}_d\right)\mathbf{w}\right)\mathrm{d}v + \int_{\Gamma}\mathbf{n}\times\left([\mu_*]^{-1}\frac{\partial\mathbf{B}_*}{\partial T}\frac{\partial T}{\partial t}\right)\mathrm{d}s = 0, \tag{55}$$

where the following notations have been used:

$$\mu_c = [\mu_*]; \quad \varepsilon_c = [\varepsilon_*]; \quad \gamma_t = \frac{\partial\gamma_*}{\partial t}; \quad \mathbf{F}_c = \mathbf{F}_q; \quad \mathbf{F}_d = \mathbf{F}_p; \quad \mathbf{E} = \mathbf{E}^{(1)} \quad \text{for } \mathbf{r}\in V;$$

$$\mu_c = \mu_0; \quad \varepsilon_c = \varepsilon_0; \quad \gamma_t = 0; \quad \mathbf{F}_c = 0; \quad \mathbf{F}_d = -\frac{\partial \mathbf{j}^{(0)}}{\partial t}; \quad \mathbf{E} = \mathbf{E}^{(0)} \quad \text{for } \mathbf{r} \in V \backslash \Omega.$$

Apply a typical finite-element space discretization [21] of Eqs. (52) and (55). In doing so, discretization of the domain V is done in such a way that the solid-surrounding interface coincides with the boundaries of the respective finite elements. As a result, a set of ordinary differential equations is obtained:

$$[L_1]\{\dot{T}_h(t)\} + [L_0]\{T_h(t)\} = \{f_T\}, \quad \{T_h(0)\} = \{T_h^0\}, \tag{56}$$

$$[M_2]\{\ddot{E}_h(t)\} + [M_1]\{\dot{E}_h(t)\} + [M_0]\{E_h(t)\} = \{f_E\}, \quad \{E_h(0)\} = \{\dot{E}_h(0)\} = 0, \tag{57}$$

written in terms of the unknown temperature $\{T_h\}$ and the electric-field strength $\{E_h\}$ in the nodes. The matrix-vector characteristics of the derived set of equations are calculated by summing up appropriate characteristics of the finite elements, whose components are given by the expressions:

$$[L_0]_{ij}^{el} = \int_{\Omega^{el}} \lambda(\nabla_1 N_i \nabla_1 N_j + \nabla_2 N_i \nabla_2 N_j + \nabla_3 N_i \nabla_3 N_j)\mathrm{d}v + \int_{\Gamma^{el}} \beta N_i N_j \mathrm{d}s,$$

$$[L_1]_{ij}^{el} = \int_{\Omega^{el}} c N_i N_j \mathrm{d}v, \quad \{f_T\}_i^{el} = \int_{\Omega^{el}} \mathbf{j}^{(1)} \mathbf{E}^{(1)} N_i \mathrm{d}v + \int_{\Gamma^{el}} \beta N_i \mathrm{d}s, \quad i, j = 1 \div n. \tag{58}$$

The matrices $[M_0]$, $[M_1]$, $[M_2]$ are composed of the following 3×3 sub-matrices

$$[M_0]_{i'j'}^{el} = \int_{V^{el}} (\mu_c)^{-1} [M_{i'j'}^{\nabla}]\mathrm{d}v + \int_{V^{el}} \gamma_t [M_{i'j'}]\mathrm{d}v,$$

$$[M_1]_{i'j'}^{el} = \int_{\Omega^{el}} \mathbf{F}_c^T [M_{i'j'}]\mathrm{d}v, \quad [M_2]_{i'j'}^{el} = \int_{\Omega^{el}} \varepsilon_c [M_{i'j'}]\mathrm{d}v, \quad \{f_E\}_{i'}^{el} = \int_{\Omega^{el}} \mathbf{F}_d^T [N]\,\mathrm{d}v, \tag{59}$$

where

$$[M_{i'j'}^{\nabla}] = \begin{pmatrix} \nabla_2 N_i' \nabla_2 N_j' + \nabla_3 N_i' \nabla_3 N_j' & -\nabla_1 N_i' \nabla_2 N_j' & -\nabla_1 N_i' \nabla_3 N_j' \\ -\nabla_2 N_i' \nabla_1 N_j' & \nabla_1 N_i' \nabla_1 N_j' + \nabla_3 N_i' \nabla_3 N_j' & -\nabla_2 N_i' \nabla_3 N_j' \\ -\nabla_3 N_i' \nabla_1 N_j' & -\nabla_3 N_i' \nabla_2 N_j' & \nabla_1 N_i' \nabla_1 N_j' + \nabla_2 N_i' \nabla_2 N_j' \end{pmatrix},$$

$$[M_{i'j'}] = \begin{pmatrix} N_i' N_j' & 0 & 0 \\ 0 & N_i' N_j' & 0 \\ 0 & 0 & N_i' N_j' \end{pmatrix}, \quad [N] = \begin{bmatrix} N_1' & 0 & 0 & N_2' & 0 & 0 & \dots & N_{n'}' & 0 & 0 \\ 0 & N_1' & 0 & 0 & N_2' & 0 & \dots & 0 & N_{n'}' & 0 \\ 0 & 0 & N_1' & 0 & 0 & N_2' & \dots & 0 & 0 & N_{n'}' \end{bmatrix},$$

$$i, j = 1 \div n'; \quad i' = 3i - 2, 3i - 1, 3i; \quad j' = 3j - 2, 3j - 1, 3j.$$

Note that the shape functions N_i for the problem (56) and N_i' for the problem (57) belong to different functional spaces and therefore, in the general case, can be different. The number of nodes n and n' in corresponding elements can also be different. In the axi-symmetric case the shape functions belong to the same functional space ($H^1(V)$) and coincide. Components of the matrix-vector characteristics of separate finite elements take the following form in this case

$$[L_0]_{ij}^{el} = \int_{\Omega_2^{el}} \lambda \left(\frac{\partial N_i}{\partial r} \frac{\partial N_j}{\partial r} + \frac{\partial N_i}{\partial z} \frac{\partial N_j}{\partial z} \right) r \mathrm{d}r \mathrm{d}z + \int_{\Gamma_2^{el}} \beta N_i N_j r \mathrm{d}\xi,$$

$$[L_1]_{ij}^{el} = \int_{\Omega_2^{el}} c N_i N_j r \mathrm{d}r \mathrm{d}z, \quad \{f_T\}_i^{el} = \int_{\Omega_2^{el}} j_{\varphi}^{(1)} E_{\varphi}^{(1)} N_i r \mathrm{d}r \mathrm{d}z + \int_{\Gamma_2^{el}} \beta N_i r \mathrm{d}\xi,$$

$$[M_0]_i^{el} = \int_{V_2^{el}} [\mu_c]^{-1} \left(\frac{\partial N_i}{\partial r} \frac{\partial N_j}{\partial r} + \frac{\partial N_i}{\partial z} \frac{\partial N_j}{\partial z} \right) r \mathrm{d}r\mathrm{d}z + \int_{V_2^{el}} \gamma_t N_i N_j r \mathrm{d}r\mathrm{d}z$$
$$+ \int_{V_2^{el}} [\mu_c]^{-1} \frac{1}{r} \left(\frac{\partial N_i}{\partial r} N_j + \frac{\partial N_j}{\partial r} N_i + \frac{1}{r} N_i N_j \right) r \mathrm{d}r\mathrm{d}z,$$

$$[M_1]_{ij}^{el} = \int_{V_2^{el}} F_c N_i N_j r \mathrm{d}r\mathrm{d}z, \quad [M_2]_{ij}^{el} = \int_{V_2^{el}} \varepsilon_c N_i N_j r \mathrm{d}r\mathrm{d}z, \quad \{f_E\}_i^{el} = \int_{V_2^{el}} F_d N_i r \mathrm{d}r\mathrm{d}z. \tag{60}$$

The Cauchy problem (53), (54) is solved by use of a unified set of single-step algorithms [23], allowing to carry out calculations for variable steps and orders of the method. In doing so, the general algorithm of ultra-weak coupling between both nonlinear time-dependent fields is involved, which allows to use different time steps for electromagnetic (Δt_E) and temperature (Δt_T) calculations [14].

The temperature and ponderomotive forces generated by the external electromagnetic field being determined, we can now consider the next stage of the problem. Namely, let us write the basic finite-element relations for the thermoplasticity problem.

3.2 Finite-element equations for thermo-mechanic problem

Consider the deformation process step by step, according to the yield theory. Starting from the known initial values at $t = 0$, the ponderomotive forces and temperature in the solid are represented by corresponding increments at each loading step in such a way that they take their final values at the end of the deformation process. Given the increments of the ponderomotive forces and temperature at each step allow to determine the displacement, strain and stress increments, which are accumulated from all previous steps. Repeating this procedure step by step, we obtain the thermomechanical time-history response of the solid.

Consider an arbitrary loading step $[t_j, t_j + \Delta t_j]$. The thermomechanical state of the solid at the beginning of this step (at time t_j) is known. Equilibrium equations at the end of the step read as follows:

$$[\mathbf{A}]^T \{\sigma\}^{t_j + \Delta t_j} + \mathbf{F}^{t_j + \Delta t_j} = 0. \tag{61}$$

Taking into account the expressions $\{\sigma\}^{t_j+\Delta t_j} = \{\sigma\}^{t_j} + \{\mathrm{d}\sigma\}$, $\mathbf{F}^{t_j+\Delta t_j} = \mathbf{F}^{t_j} + \mathrm{d}\mathbf{F}$ as well as equilibrium of the thermomechanical state at the beginning of the step, the equilibrium equations written in terms of increments take the form

$$[\mathbf{A}]^T \{\mathrm{d}\sigma\} + \mathrm{d}\mathbf{F} = 0. \tag{62}$$

Substituting the physical relations (32) and geometrical relations (33) in Eq. (62), using the standard procedure of the weighted-residuals method, and introducing finite-element approximations, we obtain the incremental displacement equilibrium equation [21]

$$[\mathbf{K}_{ep}]\{\mathrm{d}\mathbf{q}\} = \{\mathrm{d}\mathbf{R}\}, \tag{63}$$

where $\{\mathrm{d}\mathbf{q}\}$ is the global vector of increments of displacement nodes. The elastoplastic matrix $[\mathbf{K}_{ep}]$ and reaction vector $\{\mathrm{d}\mathbf{R}\}$ are calculated by summing up appropriate characteristics of finite elements:

$$[\mathbf{K}_{ep}^{(el)}] = \int_{\Omega^{el}} [\mathbf{N}]^T [\mathbf{A}]^T [\mathbf{C}]^{t_j+\Delta t_j} [\mathbf{A}] [\mathbf{N}] \mathrm{d}v, \tag{64}$$

$$\{d\mathbf{R}\}^{(el)} = \int_{\Omega^{el}} [\mathbf{N}]^T [\mathbf{A}]^T \mathbf{C}^{t_j+\Delta t_j} \{\varepsilon_T\} \mathrm{d}v - \int_{\Omega^{el}} [\mathbf{N}]^T \mathrm{d}\mathbf{F} \mathrm{d}s$$
$$- \int_{\Omega^{el}} [\mathbf{N}]^T [\mathbf{A}]^T \left([\mathrm{d}\mathbf{C}] (\{\varepsilon\} - \{\varepsilon_T\} - \{\varepsilon_p\}) + \{z\} \mathrm{d}T \right) \mathrm{d}v + \int_{\Gamma_\sigma^{(el)}} [\mathbf{N}]^T \{\mathrm{d}\mathbf{p}\} \mathrm{d}s. \tag{65}$$

Expressions (63) hold for infinitesimally small values and, in fact, represent a piece-wise linear approximation of a nonlinear deformation process. Applying these expressions for calculating finite values causes the solution to

move away from the actual equilibrium state. The residual vector of equilibrium conditions makes it possible to estimate this gap that increases with increasing load increments

$$\{\Psi\} = \{\mathbf{R}\} - \sum_{el} \int_{\Omega^{el}} [\mathbf{N}]^T [\mathbf{A}]^T \{\sigma\}^{el} \mathrm{d}v, \tag{66}$$

where the sum is taken over all finite elements; $\{\sigma\}^{el}$ denotes the values of the strength vector in the element nodes; $\{\mathbf{R}\} = \sum_j \{\mathrm{d}\mathbf{P}\}_j$ is the load accumulated during previous steps. The nonlinear Eq. (60) is solved iteratively using Newton's method [19]. The iterative procedure is constructed in such a way that a new elasto–plastic stiffness matrix $[\mathbf{K}_{ep}]$ is formed at each iteration during the j-step over the load. Then Eq. (63) is solved and the residual (66) of the equilibrium equation is calculated, the latter being added to the right-hand side of Eq. (63) at the next iteration. This matrix $[\mathbf{K}_{ep}]$ captures the instantaneous stresses and strengthening of the material.

A variable step Δt_j, $j = 0, 1, \ldots$ over the load is chosen. The increments of the displacements, strains and stresses are calculated as soon as in some point of the solid the maximum temperature rise exceeds a predefined value ΔT_j.

3.3 Approximation of material properties

As a rule, the temperature dependency of the material characteristics, deformation curves, magnetization and polarization curves are approximated by certain analytical expressions. In particular, the size of the yield surface of some steel materials is approximated in the following way [26]:

$$K^2 = \sigma_T + b(\bar{\varepsilon}_p)^m, \tag{67}$$

where σ_T is the yield limit due to ordinary elongation; b, m are material constants.

The magnetization curve for a magnetically soft ferromagnetic material is usually approximated by the expressions [19,27]

$$B(H) = \mu_0 H + b \cdot \arctan(aH), \tag{68}$$

$$B(H) = \left(\mu_0 + \frac{a}{b + H}\right) \cdot H, \tag{69}$$

where a, b are material constants.

The experimentally established relationship between periodic electromagnetic field induction and strength is commonly known as hysteresis loop. The shape of a loop is affected by the field strength and frequency, as well as by the temperature [17]. If the magnetic field strength is a harmonic function, the hysteresis loop can be approximated by the expression [19]

$$B(H) = b \cdot \arctan\left(a\left(\sqrt{1-\chi^2} \cdot H - \frac{\chi}{\omega}\frac{\partial H}{\partial t}\right)\right) + \mu_0 H, \tag{70}$$

where

$$b = B_S \frac{2}{\pi}, \qquad a = \left(\mu_p - 1\right)\frac{\mu_0}{b}, \qquad \omega = 2\pi f, \qquad \chi = \begin{cases} \dfrac{H_c}{H_{\max}}, & H_0 \le H_{\max} \\ \dfrac{H_0}{H_{\max}}, & H_0 > H_{\max} \end{cases}.$$

Here f is the frequency; H_0 is the maximum value of the magnetic-field strength. The other values needed for calculation, like the saturation induction B_s, the residual induction B_r, the coercitive force H_c, the magnetic-field strength $H_{\max}$ corresponding to hysteresis saturation, and the initial magnetic permeability μ_p, usually are reference values.

The thermal behavior of the absolute magnetic permeability of ferromagnetic steel is well approximated by the expressions [14,22]

$$\mu(H,T) = \mu_0 + (\mu(H) - \mu_0) \cdot \Theta(T), \tag{71}$$

$$\Theta(T) = \begin{cases} 1 - (T/T_C)^{\vartheta}, & T < T_C \\ 0, & T \geq T_C \end{cases}, \tag{72}$$

where T_C is the Curie temperature; ϑ is the parameter characterizing the thermal sensitivity of a material.

Taking into account expression (71), we have that Eqs. (68)–(70) take the form

$$B(H,T) = \mu_0 H + b\Theta(T) \arctan(aH)\,, \tag{73}$$

$$B(H,T) = \left(\mu_0 + \frac{a \cdot \Theta(T)}{b + H}\right) \cdot H, \tag{74}$$

$$B(H,\ T) = b \cdot \Theta(T) \arctan\left(a\left(\sqrt{1-\chi^2} \cdot H - \frac{\chi}{\omega}\frac{\partial H}{\partial t}\right)\right) + \mu_0 H, \tag{75}$$

However, these analytical expressions represent satisfactory approximations of the basic curves only for certain materials and in limited ranges of their arguments. As a result, interpolative splines constructed on real curves are preferable for these purposes. Usually splines describe well deformation curves of various complexity, as well as magnetization and polarization curves for both weak and heavy fields.

4 Induction heating of a finite cylinder. Results and discussion

The model outlined in this paper was applied to the simulation of induction heating of an electrically conductive cylinder of radius R and length $2L_i$. The cylinder is located within a coaxial inductor of radius R_i and length $2L_i$ with current density given by the expression

$$\mathbf{j}^{(0)}(r,z,t) = (0,\, J_0(r,z) \cdot (1 - \mathrm{e}^{-\eta t}) \cdot \sin(2\pi f t), 0); \quad r = R_i, |z| \leq L_i, \tag{76}$$

where f is the frequency, J_0 denotes the maximum value of the current, η is a parameter characterizing time for reach steady regime.

4.1 Nonferromagnetic and nondielectric material

Induction heating of a long cylinder assuming that elasto–plastic deformation is well described by the Tresca–Saint-Venant yield condition and that the material is ideally elasto–plastic and incompressible (Poisson ratio $\nu = 0.5$) is investigated in [18]. For the present computations we take the values of the material properties from that paper [18], namely: $\mu = \mu_0$; $\gamma = 1.35\,\mathrm{MS/m}$; $\lambda = 16.7\,\mathrm{W/(m\,K)}$; $c = 3.957\,\mathrm{MJ/(m^3\,K)}$; $\beta = 167\,\mathrm{W/(m^2\,K)}$; Young's modulus $E = 0.192 \times 10^6\,\mathrm{MPa}$; $\nu = 0.498$; coefficient of thermal expansion $\alpha_t = 17 \times 10^{-6}\,1/\mathrm{K}$; $\sigma_T = 220\,\mathrm{MPa}$; $T_0 = T_S = 273\mathrm{K}$; $J_0 = 60\,\mathrm{kA/m^2}$; $f = 30\,\mathrm{kHz}$; $R = 0.01\,\mathrm{m}$; $R_i = 0.0105\,\mathrm{m}$; $\eta = 10^5\,1/\mathrm{s}$.

To examine the convergence of the numerical procedures, the computations were carried out for various finite-element meshes, time steps and sizes of the domain V. The results obtained were analysed and compared with the results of [18].

In Fig. 1 typical finite-element meshes used are shown ($L = L_i = 0.04\,\mathrm{m}$, $R_0 = 2.5R$, $L_0 = 2L$).

In Fig. 2 are presented equivalent stress distributions $\sigma_i(r,z)$ in the cylinder at moments of time $t = t_* = 7.109\,\mathrm{s}$ (corresponding to the moment of the inductor being switched off in [18]). It can be seen that the solution in the central part of the cylinder, in fact, does not depend on the z-coordinate.

The stresses $\sigma_{rr}, \sigma_{zz}, \sigma_{\varphi\varphi}$ in the equatorial section of the cylinder crossed by the plane $z = 0$ are shown in Fig. 3 by solid lines. Dashed lines correspond to closed-form analytical solutions given in [18]. The solutions reveal good

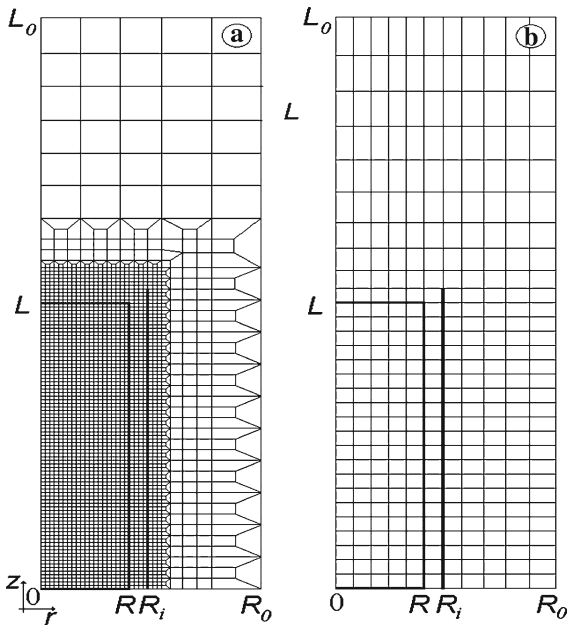

Fig. 1 Typical finite element meshes

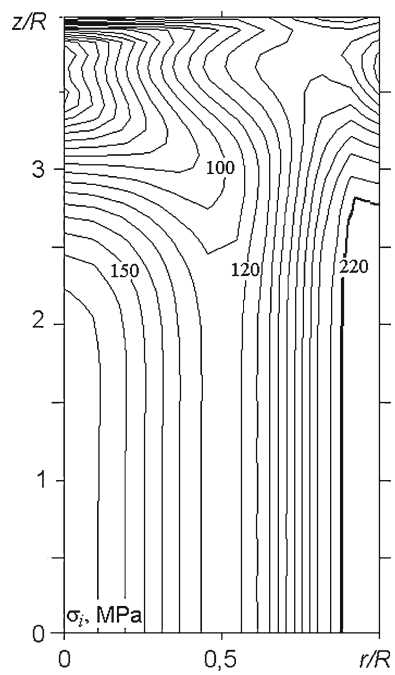

Fig. 2 Equivalent stress in the cylinder

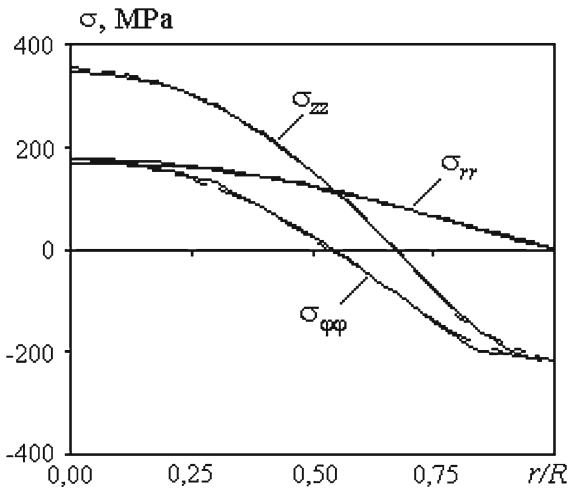

Fig. 3 Stress state in the cross-section ($z = 0$)

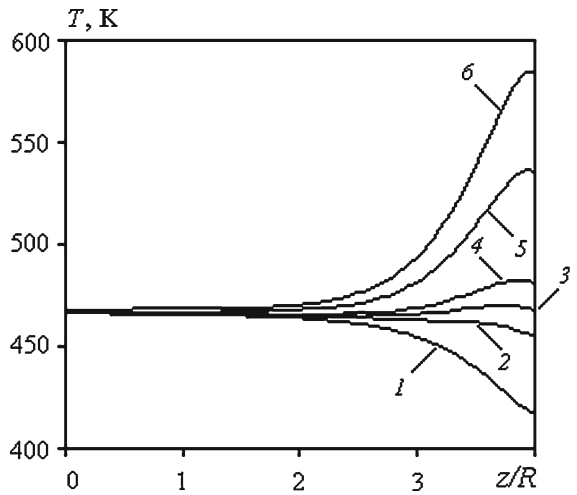

Fig. 4 Temperature on the surface for various values of the inductor length

agreement which is already obtained when five eight-node biquadratic isoparametric finite elements are taken along the cylinder radius (see Fig. 1b) and the following time steps are chosen

$$\Delta t_E = f^{-1}/16; \qquad \Delta t_T = t_*/3; \qquad \Delta t_M = t_*. \tag{77}$$

Note that the temperature and stress-state computation for this problem can be carried out with time steps $\Delta t_T \geq 10^6 \Delta t_E$ and $\Delta t_M \geq 10^6 \Delta t_E$ without loss of accuracy. This solution agrees well with that obtained for $\Delta t_M = \Delta t_T = \Delta t_E = f^{-1}/16$.

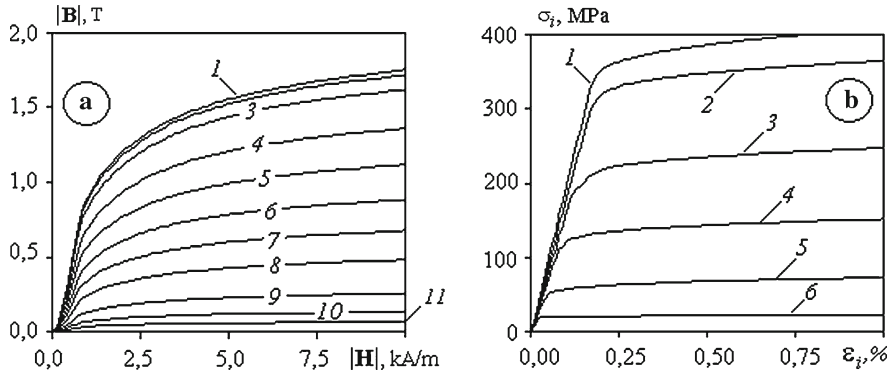

Fig. 5 Material data: magnetization (**a**) and deformation (**b**) curves at different temperatures

It should be pointed out that the substitution of the external infinite space by the finite domain V with the following parameters: $R_0 = 2.5R$, $L_0 = 2L$ (Fig. 1) does not affect the solution for the cylinder. The solutions coincide for $\forall R_0 > 2.5R, \forall L_0 > 2L$; moreover in the cross-section $z = 0$ they coincide with the analytical solution given in [18] and with the solution of the 1-D problem (47)–(49) for a long cylinder with boundary conditions

$$H_z(R,t) = 6 \times 10^4 \cdot (1 - \mathrm{e}^{-\eta t}) \cdot \sin(2\pi f t) \text{ A/m},$$

$$\lambda \frac{\partial T(R,t)}{\partial r} = \beta(T - T_S), \quad \frac{\partial H_z(0,t)}{\partial r} = 0, \quad \frac{\partial T(0,t)}{\partial r} = 0. \tag{78}$$

The numerical solutions obtained for various values of parameters R_0 and L_0 tend to differ when $R_0 < 2.5R$, $L_0 < 2L$.

In the general case, the size of the boundary-effect domain for a finite cylinder depends on the inductor length, the current magnitude, the heat-transfer conditions, etc. In Fig. 4 the temperature distributions on the cylinder surface along the z-coordinate for time $t = 7.109$ s computed at various values of inductor length L_i (0.04 (curve 1); 0.04125(2); 0.0418 (3); 0.0425 (4); 0.045 (5) and 0.05 (6)) m are shown. It can be seen that a sufficiently uniform temperature distribution along the cylinder is obtained when the inductor length exceeds the cylinder length by 5%. In this case the effect of the boundaries on the temperature distribution in the cylinder is minimal.

4.2 Soft ferromagnetic temperature-sensitive material

Consider induction heating of a soft ferromagnetic carbon-steel cylinder. Nonlinear dependencies of magnetic induction on the magnetic-field strength are shown in Fig. 5a for the temperatures 273 (curve 1), 673 (2), 773 (3), 823 (4), 874 (5), 923 (6), 958 (7), 983 (8), 1,003 (9), 1,023 (10), 1,033 (11) K. These dependencies, however, become linear with a coefficient μ_0 when the temperature is above the Curie point T_C (1,043 K) and the steel loses its ferromagnetic properties. Deformation curves for steel at the temperatures 293 (curve 1), 573 (2), 773 (3), 973 (4), 1,073 (5), 1,173 (6) K are shown in Fig. 5b.

Temperature dependencies of the electrical conductivity, heat capacity, thermal conductivity, as well as the thermal-expansion coefficient of the steel are given below. The electrical conductivity equals 6.013 MS/m at 273 K, 2.846 MS/m at 573 K, 1.233 MS/m at 873 K, 0.85 MS/m at 1,173 K and 0.76 MS/m at 1,473 K. The heat capacity equals 3.6 MJ/(m^3 K) at 273 K, 4.42 MJ/(m^3 K) at 873 K, 4.9 MJ/(m^3 K) at 1,373 K. The thermal conductivity equals 48 W/(m K) at 273 K, 48 W/(m K) at 373 K, 46.5 W/(m K) at 473 K, 44 W/(m K) at 573 K, 41.1 W/(m K) at 673 K, 38.5 W/(m K) at 773 K, 31.4 W/(m K) at 873 K, 36 W/(m K) at 973 K, 26.7 W/(m K) at 1,073 K, 25.9 W/(m K) at 1,173 K, 29.8 W/(m K) at 1,473 K. The coefficient of thermal expansion equals 11.09×10^{-6} 1/K at 273 K, 11.09×10^{-6} 1/K at 373 K, 14.02×10^{-6} 1/K at 773 K, 14.76×10^{-6} 1/K at 973 K, 1.6×10^{-6} 1/K at 1,673 K.

The cylinder ($R = 0.01$m; $L = 0.1$m) is heated by an electrical current whose variation is given in Eq. (76) ($R_i = 1.2R$; $L_i = 1.05L$; $J_0 = 1$ MA/m^2; $f = 8$ kHz; $\eta = 10^5$ 1/s; $\beta = 13$ W/(m^{2}K)). When the external layer

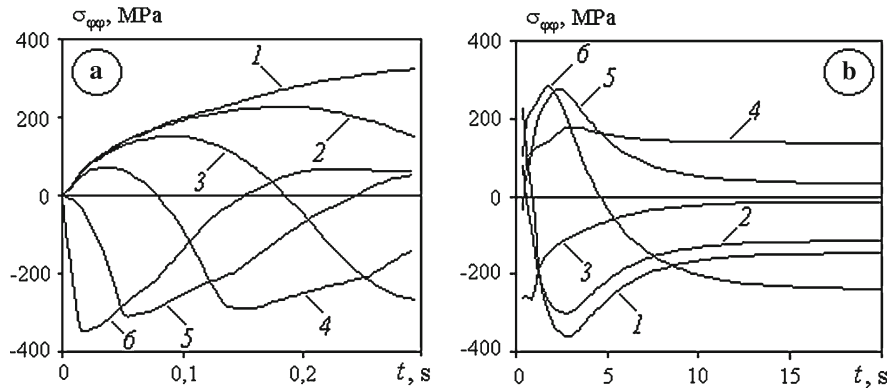

Fig. 6 Stress evolution in the cylinder during heating (**a**) and cooling (**b**)

of thickness 1.5 mm in a cross-section $z = 0$ of the cylinder is heated to the temperature $T \geq 1{,}243\,\mathrm{K}$, the current is switched off and the cylinder is cooled down due to convective heat exchange ($\beta = 10\,\mathrm{kW/(m^2\,K)}$) with the surroundings having the temperature $T_S = 293\,\mathrm{K}$ ($T_0 = T_S$).

First, let us determine the stress state in the cylinder within a model of a temperature-sensitive magnetic solid with the magnetic permeability [22] giving by

$$\mu_m(T) = \mu_0 + (\mu_{T_0} - \mu_0)\left(1 - \left(\frac{T}{T_C}\right)^6\right), \tag{79}$$

dependent on the temperature only, where

$$\mu_{T_0} = \frac{1}{H_{\max}} \int_0^{H_{\max}} \mu\left(H,\, T|_{293\,\mathrm{K}}\right)\mathrm{d}H \quad \left(\mu(H,T) = \frac{\partial\,|B(H,T)|}{\partial\,|H|}\right) \tag{80}$$

is the magnetic permeability averaged over the range of the magnetic-field strength at $T = 293\mathrm{K}$ calculated from the magnetization curve in Fig. 5a (curve 1).

Figure 6 shows the variation of the circular stresses, $\sigma_{\varphi\varphi}$, during heating (a) and cooling (b) in cylinder points $(r, 0)$, where $r = 0$ (curve *1*), 2 (2), 4 (*3*), 6 (*4*), 8 (*5*) and 10 (*6*) mm. It can be observed that at the beginning of heating in the surface layer of the cylinder the compressive stresses originate and quickly approach the yield limit. A further heating up to the Curie temperature causes the surface layer to lose its ferromagnetic properties. This means that the main heat sources and corresponding maximal compressive stresses are now located in the bulk of the cylinder, while the heated surface layer undergoes unloading. The current is switched off when the desired heating depth is reached. After that the surface layer begins to cool down and tensile stresses appear in it (see Fig. 6b, curve *6*). The bulk of the cylinder cools down less rapidly. Still, during cooling the bulk shrinks and causes the cooled surface layer to shrink quickly too, thus releasing its tensile stresses whose maximum moves inside the cylinder. This leads to the formation of residual tensile stresses in the surface layer.

In Fig. 7 we present the residual stresses σ_{rr}, $\sigma_{\varphi\varphi}$, σ_{zz} and the stress intensity σ_i (in the cross-section $z = 0$) due to plastic deformation on complete cooling of the cylinder. The boundary effect is spread over a domain equal to about six radii of the cylinder.

The effect of ponderomotive forces can be neglected in this case because the maximal stresses caused by these forces are two orders smaller than the thermal stresses (due to heat sources).

The significant changes of the magnetic permeability in the vicinity of the Curie point require an increase of the accuracy of the approximation. In particular, the numerical procedure diverges in the vicinity of the Curie point if the cylinder radius is split into 10 biquadratic elements. However, twenty biquadratic eight-node finite elements along the cylinder radius (20×200 elements in the cylinder) with time step $\Delta t_E = T_\omega/16$ suffice to ensure convergence of the solutions (in fact, 80×200 elements provide practically the same accuracy).

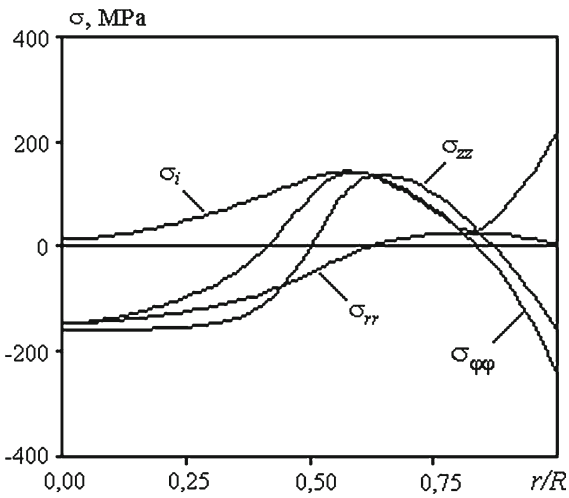

Fig. 7 Residual stresses in the cylinder

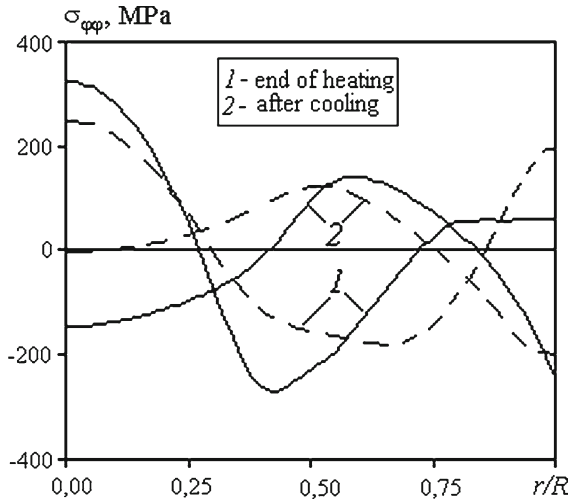

Fig. 8 Stresses in the cylinder prior to and after cooling (the dashed lines correspond to the case of temperature-independent characteristics)

The effect of thermal sensitivity of the material characteristics on the distribution of the residual stresses was examined. With this purpose in mind, the problem was also solved with temperature-independent material characteristics (their values were obtained by averaging over the heating–cooling range) and the solutions were compared. Figure 8 presents the stresses $\sigma_{\varphi\varphi}$ at the moment the inductor is switched off (curve 1) and on complete cooling of the cylinder (curve 2) when the thermosensitivity of the steel characteristics are either taken into account (solid line) or discarded (dashed line).

The effect of the temperature dependence of the steel's electrical conductivity coefficient γ and magnetic permeability μ on the electric-field strength and the temperature and stress distributions in the cylinder was also investigated [28]. Already at a temperature around 550 K, consideration of the temperature dependencies of the characteristics is crucial. It becomes even more important with further heating of the cylinder. As the temperature approaches the Curie point T_C (above 900 K), heating of the surface slows down significantly, which can be associated with the sudden drop of the magnetic permeability near the Curie point.

Residual stresses due to ferromagnetic properties (i.e., in consideration of the magnetic field's induction-strength dependence) are shown in Fig. 9. In the course of a heating–cooling process the thermomechanical properties behave in a similar way (like within the nonferromagnetic model), while the values of the residual stresses differ considerably. In particular, residual circular stresses differ more than twice.

Consideration of the nonlinear magnetic-field induction-strength dependence requires significantly higher computer resources (see [28]) in the case of coupled thermo-electro-dynamic problems. Besides, reference data on induction-strength nonlinearity of many ferromagnetic materials are not available. As a result, independent values of the magnetic permeability are normally used in electromagnetic computations for ferromagnetic materials. However, the problem of computating this independent value is still of importance.

Results for the time it takes to heat the cylinder to the required temperature as predicted by the two considered models differ nearly by a factor of two; 0.289 s is the prediction by the nonferomagnetic model (with magnetic permeability determined by expressions (79)–(80)) while the model for a ferromagnetic solid gives 0.159 s. Because of this, a set of computations have been carried out to find out the magnetic permeability

$$\mu_g(T) = \mu_0 + (\mu_{T_g} - \mu_0)\left(1 - \left(\frac{T}{T_C}\right)^6\right) \tag{81}$$

independent of the magnetic-field strength, which would predict the same heating time to a given temperature by both models.

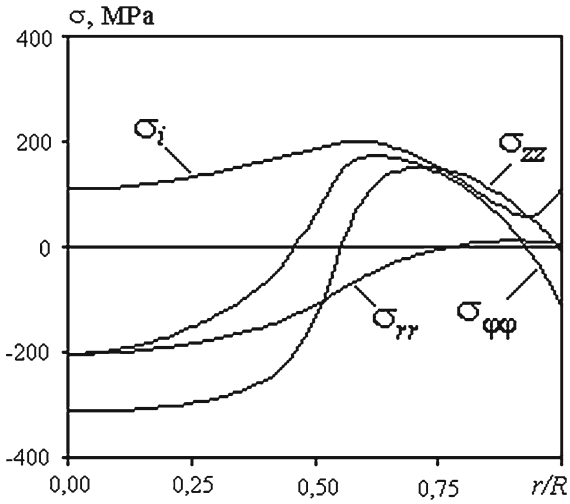

Fig. 9 Residual stresses in a ferromagnetic cylinder

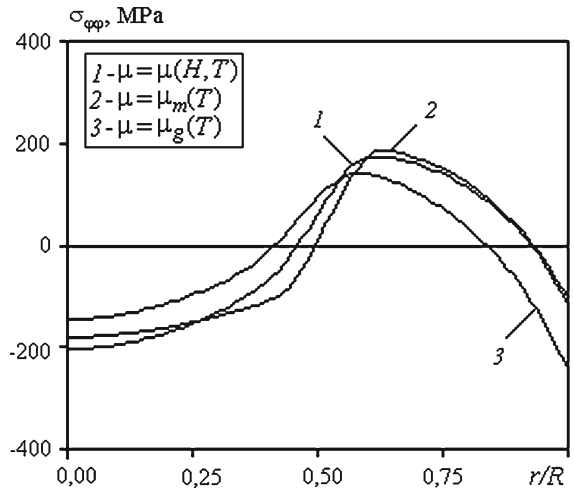

Fig. 10 Residual circular stresses predicted by different models

Figure 10 illustrates the distribution of the residual stresses $\sigma_{\varphi\varphi}$ in the cylinder during the entire cooling process. Curve 1 was obtained by the model of a ferromagnetic material, while curves 2 and 3 were obtained by the magnetic-material model with respective magnetic permeabilities μ_m, Eq. (79), and μ_g, Eq. (81) which depend on the temperature only. It can be seen that it is possible to obtain such magnetic permeabilities that would ensure accurate stresses in the ferromagnetic cylinder. In the case under consideration, μ_{T_g} is the averaged value of the magnetic permeability for $H_{\max} = 0.475\,\text{MA/m}$, while μ_{T_0} is obtained for $H_{\max} = 1\,\text{MA/m}$.

Therefore, an inverse problem regarding the determination of the averaged magnetic permeability of ferromagnetic solids using expressions like (81) can be used if the time needed for heating up to a certain temperature is known. This would allow to get accurate enough estimates of residual stresses in ferromagnetic solids.

4.3 Magnetically hard ferromagnetic material

Here we check if the approach developed here is applicable in the case of ferromagnetic solids having hysteresis dependence of magnetic-field induction upon the strength. Let us consider the problem of determining such values of the induction frequency f and cooling heat-transfer parameter β which provide the shortest time of heating up the cylinder to the temperature T_g following a cooling process conducted in a way that ensures that the maximal stresses do not exceed a permissible level σ_*.

Suppose that the cylinder is made of an alloy characterized by a wide-enough dynamic hysteresis loop in a harmonic electromagnetic field. Figure 11 shows the dependence of the magnetic induction on the strength for that alloy for the temperatures 293 (curve *1*), 823(*2*), 973(*3*), 1.073(*4*), 1.123 (*5*) K. At the Curie point T_C (1.123 K) the alloy losses its ferromagnetic properties and the induction-strength dependence becomes linear with coefficient μ_0. The magnetic-permeability dependence on the magnetic-field strength and temperature is approximated by Eq. (75) ($H_c = 55\,\text{kA/m}$; $H_{\max} = 240\,\text{kA/m}$; $B_s = 1.2\,\text{T}$; $\mu_p = 151$; $f = 500\,\text{Hz}$).

The following values of the material parameters were used in the numerical simulations:

$$\gamma = 1.12\,\text{MS/m}, \quad \lambda = 72.4\,\text{W/(m K)}, \quad c = 1.724\,\text{MJ/(m}^3\,\text{K)}, \quad T_0 = T_S = 273\,\text{K},$$
$$\beta = 13\,\text{W/(m}^2\,\text{K)} \quad \text{(during heating)}, \quad T_g = 1,323\,\text{K}, \quad R = 0.01\,\text{m}, \quad J_0 = 240\,\text{kA/m}^2,$$
$$E = 196 \times 10^3\,\text{MPa}, \quad \nu = 0.281, \quad \alpha_t = 17 \times 10^{-6}\,1/\text{K}, \quad \sigma_* = 100\,\text{MPa}.$$

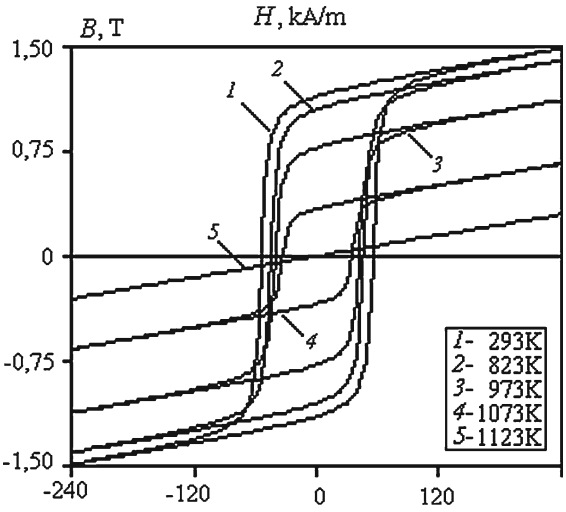

Fig. 11 Dependence of magnetic induction on the strength

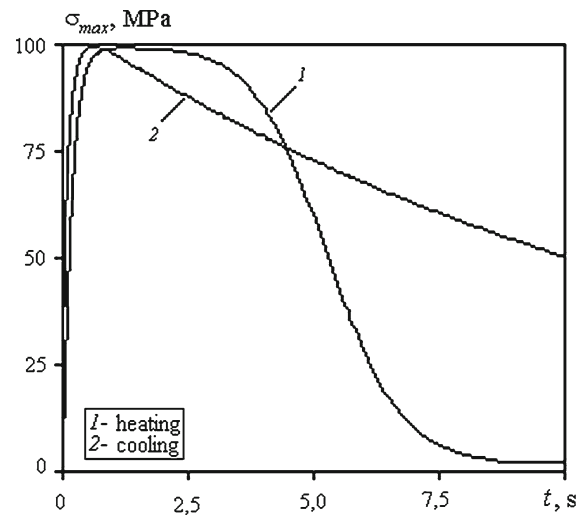

Fig. 12 Evolution of maximal stresses during heating and cooling

The values of the magnetic permeability in the points where electrodynamic equations have been integrated numerically are computed by the following approximate expression

$$\mu\left(|\mathbf{H}|,\ T\right)=\mu_0+\frac{ab\Theta\left(T\right)}{\sqrt{1-\chi^2}\left(1+a^2\left(\sqrt{1-\chi^2}\cdot|\mathbf{H}|-\frac{\chi}{\omega}\frac{\partial|\mathbf{H}|}{\partial t}\right)\right)}. \tag{82}$$

The numerical investigations reveal that the analytical approximation (82) provides better results than direct numerical differentiation when the magnetic-field strength is small. When the magnetic-field strength is large (high amplitude), the results practically coincide.

Immediately after the start of heating, the stresses reach their maximum values. As heating continues, they gradually drop. A similar trend is observed during cooling. On analyzing induction heating at various frequencies for various cooling conditions, we established that the maximum stresses approach a permissible level σ_* when the frequency is 530 Hz and the heat-transfer coefficient during cooling is 655 W/(m^2 K). This is illustrated in Fig. 12.

At the beginning of heating, the accumulated heat sources due to remagnetization are comparable with Joule heat sources (see Fig. 13). Therefore they should be taken into account when computating the temperature (see Fig. 14) and the stress state in a cylinder. Heating of the cylinder surface considerably slows down after passing the Curie point when the material loses its ferromagnetic properties. Subsequent heating is exclusively due to Joule heat sources which diminish considerably too.

Numerical investigations also showed that the effect of ponderomotive forces generated by a magnetic-field strength of about 10^5–10^6 A/m on the stress state of the solids considered above is negligible.

5 Conclusions

In this paper an approach has been developed to model the thermomechanical processes in polarizable and magnetizable electroconductive solids subjected to an external electromagnetic field. This approach provides a more adequate prediction of the behavior of solids made of magnetic materials in a wide temperature range. It also makes possible to take into account the behavior during induction heating, in particular, to estimate the residual stresses, which is the critical parameter in developing product operating regimes. It can also be of use when optimum (by certain criteria) induction-heating regimes have to be developed for electroconductive materials, these criteria being

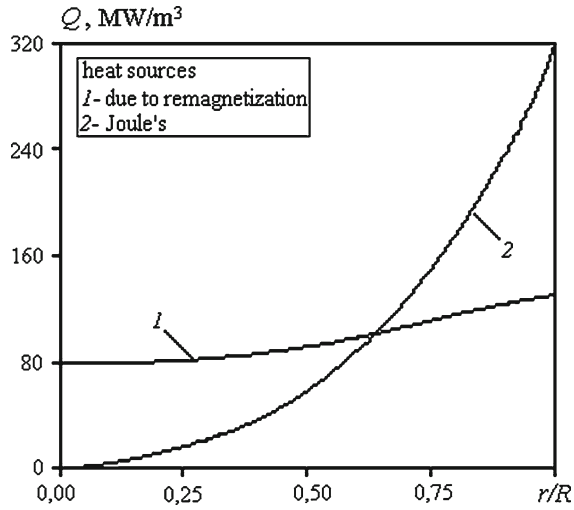

Fig. 13 Heat generated in the cylinder at the beginning of heating

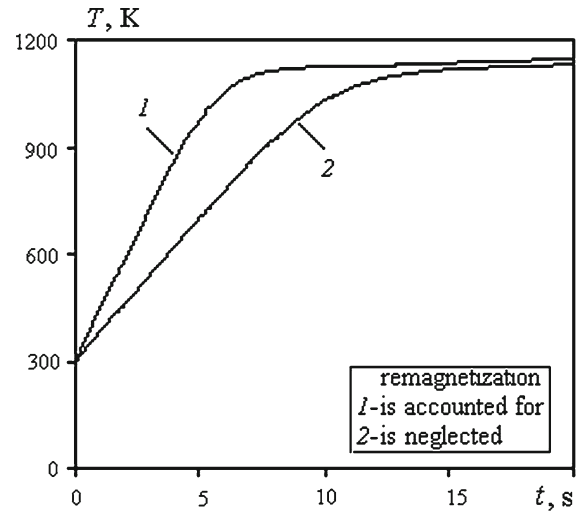

Fig. 14 Temperature evolution at the cylinder surface

particularly the uniformity of heating, minimization the heating time at given constraints on the stresses, minimal stress deviations from some prescribed values, etc. In doing so, these values can be controlled by the inductor shape and by current frequency and magnitude.

In modelling high-temperature induction heating, the thermosensitivity of the material properties should necessarily be taken into account. Otherwise, deviations of the obtained results from the actual ones become unacceptable.

If hysteresis dependence of the magnetic-field induction upon the strength is present during the computation of the thermomechanical parameters during induction heating, the heat sources due to remagnetization should not be neglected. In such cases, inaccurate temperature fields and stress states will be obtained.

The effect of the ponderomotive forces (resulting from a magnetic-field strength about 10^5–10^6A/M) on the thermomechanical behavior of electroconductive solids with parameters as considered above and frequencies outside resonance, can be neglected.

References

1. Golovin HF, Zamiatin MM (1990) High frequency thermal treatment. Leningrad 71 (in Russian)
2. Turowski J (1993) Technical electrodynamics. Warsaw, pp 30:66–68 (in Polish)
3. Bodart O, Boureau A-V, Touzani R (2001) Numerical investigation of optimal control of induction heating processes. Appl Math Model 25:697–712
4. Chaboudez C, Clain S, Glardon SR, Mari D, Rappaz J, Swierkosz M (1997) Numerical modelling in induction heating for axisymmetric geometries. IEEE Trans Magn 33(1):739–745
5. Dolezel I, Barglik J, Sajdak C, Skopek M, Ulrych B (2003) Modelling of induction heating and consequent hardening of long prismatic bodies. Int J Comput Math Electr Electron Eng 22(1):79–87
6. Dolezel I, Barglik J, Ulrych B (2005) Continual induction hardening of axi-symmetric bodies. J Mater Process Technol 161:269–275
7. Favennec Y, Labbe V, Bay F (2003) A numerical modeling example in multiphysics coupling: analysis and optimization of induction heating processes. Mecan Ind 4:347–355
8. Kawaguchi H, Enokizono M, Todaka T (2005) Thermal and magnetic field analysis of induction heating problems. J Mater Process Technol 161:193–198
9. Nemkov V, Goldstein R (2003) Computer simulation for fundamental study and practical solutions to induction heating problems. Int J Comput Math Electr Electron Eng 22(1):181–191
10. Librescu L, Hasanyan D, Qin Z, Ambur R (2003) Nonlinear magneto-thermo-elasticity of anisotropic plates immersed in a magnetic field. J Therm Stresses 26(11–12):1277–1304

11. Hasanyan D, Librescu L, Qin Q, Ambur DR (2005) Magneto-thermo-elastokinetics of geometrically nonlinear laminated composite plates. Part I: foundation of the theory. J Sound Vibration 287(1–2):153–175
12. Qin Z, Hasanyan D, Librescu L, Ambur DR (2005) Magneto-thermo-elastokinetics of geometrically nonlinear laminated composite plates. Part II: vibration and wave propagation. J Sound Vibration 287(1–2):177–201
13. Hasanyan D, Librescu L, Qin Z, Young RD (2005) Thermo-elastic cracked plates carrying non-stationary electrical current. J Therm Stresses 28(6–7):729–745
14. Bay F, Labbe V, Favennec Y, Chenot JL (2003) A numerical model for induction heating processes coupling electromagnetism and thermomechanics. Int J Numer Methods Eng 58:839–867
15. Pantelyat IG (1999) Numerical analysis of impulse electromagnetic fields in soft ferromagnetic materials. Int J Appl Electromagn Mech 10:185–192
16. Pantelyat IG, Zgraja J (1999) Inductive heating of large steel disks: coupled electromagnetic, thermal and mechanical simulation. Int J Appl Electromagn Mech 10:303–313
17. Tamm IE (1976) The basis of the electricity theory. Moscow, pp 397–403 (in Russian)
18. Podstryhach YaS, Burak YaYo, Gachkevich AR, Cherniavskaya LV (1977) Thermoelasticity of electrically conductive solids. Kiev, Naukova Dumka, pp 11–12, 126–132 (in Russian)
19. Gachkiewich A, Kasperski Z (1999) Models and mathematical methods in boundary value problems for the thermomechanics of electrically conducting solids. Politechnika Opolska, Opole, pp 94–95 (in Polish)
20. Allen DH, Heisler WE (1981) A theory for analysis of thermoplastic materials. Comp Struct 13:129–135
21. Zienkiewicz OC, Taylor RL (2000) Finite element method. Butterworth Heinemann, London
22. Skoczkowski T, Kalus M (1989) The mathematical model of induction heating of ferromagnetic pipes. IEEE Trans Magn 3:2745–2750
23. Zienkiewicz OC, Wood WL, Nine NW (1984) A unified set of single step algorithm. Part 1: general formulation and applications. Int J Num Methods Eng 20:1529–1552
24. Zienkiewicz O, Morgan K (1986) Finite elements and approximation [Russian translation]. Mir, Moscow, pp 40–92 (in Russian)
25. Duvaut G, Lions J-L (1980) Inequalities in mechanics and physics. Nauka, Moscow (in Russian)
26. Morozow EM, Nikishkov GP, Chernysh TA (1986) Nonisothermal model of elasto-plastic solid with combined strengthening law. Model application for МКэ-расчета for solid with cracks. Analytical and numerical methods in solving plastic and viscoplastic boundary problems. Ural scientific center, Academy of Sciences of USSR, Sverdlovsk, pp 87–94 (in Russian)
27. Bossavit A, Verite JC (1983) The Trifou' code: solving the 3-D eddy-currents problem by using H as state variable. IEEE Trans Magn 19(6):2465–2470
28. Drobenko B, Hachkevych O, Kournyts'kyi T (2007) A mathematical simulation of high temperature induction heating of electroconductive solids. Int J Heat Mass Transf 50:626–624